Title: Additive Manufacture of Composite Soft Pneumatic Actuators

Authors:

Oisín Byrne[1,2*], Fergal Coulter[1,3*], Mark Glynn[4], James F.X. Jones[4], Aisling Ní Annaidh[1], Eoin D. O'Cearbhaill[1,2**], Dónal P. Holland[1**]

Institutions/Affiliations:

[1] School of Mechanical and Materials Engineering, University College Dublin, Belfield, Ireland

[2] SFI Centre for Research in Medical Devices (CÚRAM)

[3] Complex Materials, Department of Materials, ETH Zurich, Zurich, Switzerland

[4] School of Medicine, University College Dublin, Belfield, Ireland

* Joint First Co-Authors

Oisín Byrne (**Email:** oisin.byrne@ucdconnect.ie)

Dr. Fergal Coulter (**Email:** fergal.coulter@ucd.ie)

**Authors of Correspondence

Dr. Dónal Holland **(Tel:** +353-1-7161910 **Email:** donal.holland@ucd.ie)

Dr. Eoin O'Cearbhaill **(Tel:** +353-1-7161715 **Email:** eoin.ocearbhaill@ucd.ie)

Address of Correspondence

School of Mechanical & Materials Engineering

University College Dublin

Belfield, Dublin 4, Ireland

Keywords: soft pneumatic actuators, composite material actuators, additive manufacturing

Abstract

This paper presents a direct additive manufacturing method for composite material soft pneumatic actuators that are capable of performing a range of programmable motions. Commonly, molding is the method used to manufacture soft fluidic actuators. This is material, labor, and time intensive, and lacks the design freedom to produce custom actuators efficiently. This paper proposes an alternative, semi-automated method of designing and manufacturing composite soft actuators. An affordable, open-source desktop 3D printer was modified into a four-axis combined Fused Deposition Modelling and Paste Extrusion printer. A Grasshopper3D algorithm was devised to implement custom actuator designs according to user inputs, resulting in a G-Code print file. Bending, contracting, and twisting motion actuators were parametrically designed and subsequently additively manufactured from silicone and thermoplastic elastomer (TPE) materials. Experimental testing was completed on these actuators along with their constitutive materials. Finite Element Models were created to simulate the actuators' kinematic performance. Having a platform method to digitally configure and directly additively manufacture custom motion composite soft actuators has the potential to accelerate the development of more intricate designs, and lead to potential impacts in a range of areas including in-clinic personalization of soft assistive devices and patient-specific biomedical devices.

1) Introduction

Fiber-Reinforced (FR) soft fluidic actuators have attracted significant interest due to their large amplitude multi-degree-of-freedom motions[1,2], their ability to be "mechanically programmed"[3], and their inherently compliant and lightweight composition[2]. FR actuators consist of a tube-like elastomeric bladder, combined with circumferentially wrapped strain limiting reinforcement fibers. FR actuators that execute twisting, bending, extending, or expanding motions have been studied[1,4-7], and have many potential applications.

Biomimetic multi-degree-of-freedom actuators that comprise selective reinforcement have been explored[8-10]. Connolly *et al.* investigated a multi-segment robot that executes combined motions in confined space[3]. Emerging medical device applications show there is a need for soft actuators that can be tailored to a wide range of specific tasks; in particular, to function in novel soft robotic devices such as the Cardiac-Assistive-Sleeve[11-13], steerable catheters[14], micro-scale surgical graspers[15-17], or The Bio-Design Glove[2].

Multi-step molding techniques are the predominant manufacturing method of soft actuators[1,6,9,12,18,19]. Molding facilitates repeated copies of the same actuator to be produced, but has no flexibility to design iterations and can be time and resource expensive (Fig. 1(i)). Additive Manufacturing (AM) has been investigated as an alternative to molding and manual fiber orientation[19-21]. Peele *et al.* presented a Digital-Mask-Projection-Stereolithography (DMP-SLA) system using a photo-curable elastomer material[22]. Yap *et al.* presented a Fused Deposition Modelling (FDM) method using NinjaFlex[23]. PolyJet co-printing methods have been demonstrated using industrial printers[24,25]. "The Octobot" revealed an entirely soft embedded (EMB-3D) printing method[26].

Collectively, these methods have largely focused on direct printing of single material bending type actuators, limiting their applicability. There remains a need to print composite structures so that FR-style and other multi-material actuator types can be produced[10,20,27]. Coulter *et al.* described a method whereby a soft silicone balloon is fabricated by spray, then inflated. This shape is then 3D scanned, to allow a harder silicone auxetic pattern to be extruded over the surface using a custom four-axis printer[28]. Such a system could be adapted to fabricate FR-style tubular soft actuators.

In this paper; a method to fabricate multi-motion composite soft pneumatic actuators through direct additive manufacture is presented (Fig. 1(ii)). A streamlined four-axis printing system compatible with elastomeric materials of different tensile strengths is described. The steps involved in applying modifications to a desktop 3D printer are outlined. The workings of a Grasshopper3D algorithm that facilitates rapid actuator customization through intuitive input parameters is explained. The flexibility of this design and AM system is highlighted by illustrating three directly printed actuator designs,

namely, bending, contracting, and twisting actuators. The motions of the actuators are studied through experimental testing conducted at increasing fluidic pressures. Axial-strain is used to quantify the degree of longitudinal shortening for the contraction design, angle-of-twist is used for the twisting design, and radius-of-curvature is used for the bending actuator. The responses of the actuators are simulated numerically using Finite Element Analysis and validated experimentally in order to gain an understanding of the multi-layer interactions between the compliant silicone and stiffer TPE reinforcement layers.

2) Actuator Design and Fabrication

2.1 Printer Design

A modified Ultimaker-Original open-source printer was used for composite printing of the tubular actuators. Modifications to the printer included the addition of a paste extrusion printhead (Fig. 2(c)). Extrusion printing involves applying pneumatic pressure to a piston which extrudes a paste through a dispensing tip. In this case, the paste was a viscous room-temperature-vulcanization silicone (Dragon Skin 10, Smooth-On Inc., Macungie, PA), and the dispensing tip was a 20-gauge (0.6mm ID) luer lock nozzle. For simplicity and cost effectiveness, an open-loop control strategy was implemented for this printhead. The output extrusion was controlled using a solenoid valve (W0215000151, Metal Works Pneumatic Ltd., Milton Keynes) attached between the air supply and material (Fig. 2(b)). To prevent over-extrusion, an exhaust port on the valve was used to vent pressure from the dispensing syringe at the end of a printed line. Extrusion rate was controlled by an analogue pressure regulator (FM-30-02-W, SDPC, Set Press. 0.05-0.85MPa), (Fig. 2(a)). A direct-drive FDM "Wade" extruder[29] was incorporated to print thermoplastic elastomer (TPE) filament, ("Ninjaflex", thermoplastic polyurethane, ink3D.ie, Dublin). The extruder body itself was 3D printed, and then combined with the standard hot-end parts[30], including the 0.4 mm hot-end nozzle (Fig. 2(d)). As TPE is soft and easily kinked, the direct-drive extruder served to increase filament traction and therefore print speed, when compared to the native Bowden-drive system. The final modification included the addition of a

rotational fourth-axis, with a cylindrical mild steel mandrel forming the printing substrate. A Nema-17 stepper motor, mounted on an opposing pair of angle aluminum brackets was used to actuate this axis. This motor was coupled directly to the mandrel (Fig. 2(e)). Although a rotational fourth-axis is not standard on the Ultimaker, one was implemented by means of a “hack”. The Marlin firmware is designed to support multiple extruders and it was one of these which was repurposed to actuate the fourth axis.

2.2 Actuator Fabrication

2.2.1 Actuator Composition

The actuators are composed of a compliant soft silicone matrix combined with a stiffer TPE reinforcement layer. The matrix is composed of two silicone layers; the bladder and the skin layer which are chemically fused in the gaps present between the TPE strands. The TPE layer functions the same as the inextensible fibers in FR type actuators. Fig. 3 illustrates the actuators’ composition by means of an exploded view.

2.2.2 Actuator Design

The actuators were designed using a custom Grasshopper3D algorithm. Grasshopper3D is a parametric graphical programming tool, available as a plug-in for the CAD package Rhino3D. Fig. 4 illustrates a schematic of the algorithm’s workings. The algorithm is partitioned into an interface and a back-end for ease of use. The algorithm is integrated whereby designing and “slicing” are combined, removing the need to use the dedicated intermediate slicing software commonly found in AM work-flows. To configure an actuator, the designer need only interact with the front-end of the algorithm where ten user-inputs are available to tune the actuator design (Fig. 4(a)). The type of actuator must be selected which dictates the pattern of reinforcement that will be created. Contract, bend, and twist options are available. Input parameters controlling the properties of each actuator layer must also be defined. These inputs are easily adjusted using intuitive number sliders. The complete list of actuator parameters is outlined in Table 1.

The back-end of the algorithm reads the user inputs, performs a series of repetitive tasks, and writes to an output G-Code file without requiring user manipulation (Fig. 4(b)). The first actuator layer is the silicone bladder which is created using a dedicated section of the algorithm. To generate G-Code for this layer, simple linear move commands are used to move the printhead over and along the rotating mandrel. In addition, M-commands control the solenoid valve. The final skin layer is generated by re-using this portion of the algorithm. Creating G-Code for the TPE reinforcement layer is achieved by translating the user inputs into rectangular grids corresponding to the top, middle, and bottom actuator reinforcement sections respectively (Fig. 4(b_i)). If a twisting or bending actuator is chosen, the middle grid must be manipulated, e.g. for a twisting actuator, the middle section grid will be skewed by a desired skew angle θ. A raster style continuous toolpath is then generated connecting all the vertices of the grids. Ordering of these vertices is critical and is achieved using data-set manipulation components (Fig. 4(b_{ii})). To maximize the quality of prints, print jobs are programmed to run without lifting or stopping the printhead or traversing over print-lines twice. If a multi-layered print is desired, the toolpath is duplicated and offset in the Z-direction (Fig. 4(b_{iii})). To calculate the quantity of material to extrude (distance/mm) for a highly variable toolpath requires the algorithm to be automated as this is not feasible to achieve through manual means for complex toolpaths. The algorithm achieves this by extracting the start and end-points for each rectilinear line segment of the toolpath. The line segments are sub-divided into small (<1mm) lengths (Fig. 4(b_{iv})). An extrude quantity is calculated and assigned to each sub-division. The printer was controlled using absolute positioning in this work including the extrusion quantity E. Therefore, addition is performed on the individual extrusion quantities to inform the printer the absolute quantity of material to extrude for each sub-division. The X, Y, Z Cartesian coordinates of the toolpath vertices are decomposed and combined with their corresponding extrusion quantities, and feed rates. Y coordinates are converted to E2 equivalent which is addressable in the firmware as the rotational axis. The values are concatenated and output in the syntax of CNC G-Code which is understood by the firmware and can be printed (Fig. 4(c)). The graphical representations of each back-end function are illustrated in Fig. 4(d_{i-iv}).

2.2.3 Actuator Printing

To prepare for printing, Plat-Cat cure accelerator (Smooth-On Inc., Macungie, PA), was added 4wt. % to part-A of Dragon Skin-10. This addition halved the pot life to 10 mins and increased the silicone viscosity which aided print morphology retention. Mixing of part A and B of Dragon Skin-10 was achieved manually in this work, however this can be automated in future work[31]. The mixture was inserted into a vacuum chamber for 4 mins until no air bubbles emerged from the surface. Once degassed, the mixture was transferred into the syringe barrel and mounted in the printer. The material and printing parameters are outlined in Table 2, and 3 respectively. Fig. 5 illustrates the three-layer additive manufacture of a twisting actuator. A 2mm thick Dragon Skin-10 bladder layer is the first constitutive layer, which was formed by cold extruding onto a 14 mm mandrel using the paste extrusion printhead (Fig. 5(a)). An extrusion pressure of 500 kPa was empirically determined for this layer providing a controlled and uninterrupted material flow from the dispensing tip. A mandrel rotational speed of 20 rpm was found to be optimum in assisting self-levelling of the mixture. The inherent high viscosity of Dragon Skin-10 meant that no additional rheology modifiers were necessary. Once bladder extrusion was complete, the mandrel continued to rotate to prevent dripping. Heat from an infrared light bulb was intermittently applied at this point to accelerate the platinum-catalyzed silicone cure.

TPE reinforcement comprises the second constitutive layer (Fig. 5(b)). The TPE filament was printed using FDM where the material flow was in the same direction as the tensile stretching[23]. Adherence issues arose when depositing TPE on an elastomeric substrate due to the material's soft nature. This was resolved by implementing the following measures: i) using a direct-drive printhead; ii) over-extruding by 50% to ensure sufficient material flow; iii) a layer height of 0.5 mm; iv) reducing the print speed to 100 mm per minute to prevent the nozzle tugging on the filament particularly during cornering; and v) using an extrusion temperature of 235°C. These measures resulted in an increased area for the filament to adhere to the silicone. A final 2mm silicone skin layer was extruded in a single pass over the previous two layers at 500 kPa (Fig. 5(d)). This layer served to add structural integrity

to the actuator and prevent relative displacement of the TPE fibers. Printing of bending and contracting actuators involved a similar process, in which only the geometry of the TPE reinforcement layer varied.

3) Actuator Characterization

3.1 Actuator Testing

The kinematics of the bending, contracting and twisting actuators were experimentally characterized using an evaluation platform and methods similar to that of Polygerinos et al.[32]. To test an actuator, it was clamped on a rigid 3D printed fitting that incorporated an airline attachment port. The actuator was aligned parallel to the image plane of a high-resolution tripod mounted camera (EOS 700D DSLR, Canon Inc., NY) to minimize lens distortion. The camera was positioned so that the lens centerline height was coincident with the actuator centerline height and at a fixed stand-off distance from the actuators during testing. Circular markers (2mm ∅) were placed at strategic locations on the actuators surface to facilitate image processing in ImageJ (National Institute of Health, MD) (Fig. 6(b)). Using high resolution images, and ensuring the markers were small relative to the actuators size facilitated more accurate centroid evaluation during image analysis. A ruler was positioned in the scene parallel to the actuator to serve as a spatial calibration reference. The actuators were tested at increasing constant pressure increments (17.24kPa) using a manually operated low pressure regulator (AR20-F02-1N-B, SMC, Set Press: 0.02-0.2 MPa). Prior to testing, the desired pressure set-point was verified using an inline pressure transducer (ASDX-AVX100PGAA5, Honeywell, +/-2% accuracy). At each steady-state pressure value, a photograph was taken and the test was repeated three times to assess repeatability and obtain an average result. Once the camera was positioned for the first repetition of the experiment, it remained fixed for the following two repetitions to prevent misalignment errors which could diminish the accuracy of subsequent tests. Kinematic characterization was completed in ImageJ by calibrating the size of each photo, and analyzing displacements of the centroids of the marker array relative to their reference points. Axial strain (ε) was quantified for the contraction actuator by calculating the change in length between two end markers on the actuator relative to their

original length; angle of twist (τ) was determined for the twisting actuator using the method described by Connolly et al.[3], and radius of curvature (R) was determined for the bending actuator using an ImageJ plug-in macro[33].

3.2 Material Characterization

Uniaxial tensile tests were performed on Dragon Skin-10 and longitudinally printed TPE dumbbell samples using a universal testing machine (H50KS, Hounsfield, 1kN load cell). The specimens were tested according to ISO 37:2011. Dumb-bell dimensions were 115 mm (L) $\times$ 25 mm (W), 6.2 mm (Narrow Portion Width) $\times$ 2 mm (T). Testing was conducted at a speed of 500mm/min. Tensile testing was the mode chosen to characterize the materials as it constitutes a significant portion of the total material stress during actuator inflation. Nominal stress-strain data was collated from three samples of each material and averaged to obtain a representative result (Fig. 7).

3.3 Finite Element Modelling

Finite Element (FE) models were developed for each actuator design using Abaqus/CAE (V6.14, Dassault Systèmes®, RI). These models were developed primarily to simulate and predict the motion response of each actuator type under fluid pressurization. They also served as a design tool to visualize the location of stress concentrations. Experimental stress-strain data for TPE (0-33% strain) and Dragon Skin-10 (0-630% strain) was utilized for curve fitting using the built-in curve-fitting tool in ABAQUS CAE. Assuming incompressibility, appropriate strain energy functions (SEF) were selected based on model stability and closeness of fit. The selected constitutive model for Dragon Skin-10 was an Ogden model, N=3 (R^2 = 0.999), and for TPE a Polynomial model, N=2 ($R^2 = 0.999$). The model parameter values are outlined in Table 4; the mathematical formulations of each are represented by Eq. 1, 2[34]. The Ogden model expresses the SEF in terms of principal stretches, $\bar{\lambda}_1, \bar{\lambda}_2, \bar{\lambda}_3$ and temperature dependent material parameters α_i and μ_i. The Polynomial model expresses the SEF in terms of two strain invariants $\bar{I}_1$, and $\bar{I}_2$, where C_{ij} are temperature dependent material parameters.

Ogden, N=3: $$W = \sum_{i=1}^{N} \frac{2\mu_i}{\alpha_i^2} (\bar{\lambda}_1^{\alpha_i} + \bar{\lambda}_2^{\alpha_i} + \bar{\lambda}_3^{\alpha_i} - 3) \quad (1)$$

Polynomial, N=2: $$W = \sum_{i+j=1}^{N} C_{ij} (\bar{I}_1 - 3)^i (\bar{I}_2 - 3)^j \quad (2)$$

Three-dimensional solid models for each of the actuator layers were created using Inventor® (Professional 2018, Autodesk Inc., CA) and then imported into Abaqus where surface-sets were defined on each. The parts were assigned materials (See Table 4) and meshed using 10-node hybrid quadratic tetrahedral elements (C3D10H). The number of nodes and elements for each part are outlined in Table 5. To capture the overall actuator stiffness, the three individual actuator layers were incorporated. This multi-layer structure added complexity to the models as the physical interactions between each layer must be explicitly defined. In addition, both materials exhibit non-linear elastic behavior and large deformations, making the choice of surface interaction non-trivial. The combination of constraints implemented was dependent on the type of actuator being modelled; a single master model valid for the three actuator types was not defined due to variations in the modes of actuator deformation, namely torsion, bending, and tension. In bending and contraction, the bladder was tied to both the TPE and the outer skin using a tie constraint. This meant that there was no relative motion between these layers. The contact interaction between TPE and skin layers was defined as surface-to-surface finite sliding because it allows for arbitrary separation, sliding and rotation between the surfaces. In twisting, surface-to-surface finite sliding was implemented across all layers to avoid numerically (and artificially) over-constraining the model elements. Where a penalty friction formulation was applied, the coefficients of friction were determined experimentally ($\mu_k, \text{Silicone, TPE} = 0.85$, $\mu_k, \text{Silicone, Silicone} = 1.027$). The combinations of constraints used are outlined in Table 5. An encastre boundary constraint was applied on the fixed end of the actuators to represent their attachment to the pneumatic fitting, the fitting itself was excluded for simplicity. A static step with a linearly ramped pressure load was applied to the cavity of the actuators. Simulations were executed using the Abaqus Standard solver and output requests were at time points corresponding to discrete experimental constant pressure values for computational efficiency.

4) Results

Numerical results correlated closely with experimental results for the three actuator types. The deformations of the individual actuators are plotted in Fig. 6(d). The first actuator experimentally and numerically characterized was the contraction design. Upon fluid pressurization, this actuator expands radially and shortens axially. To maximize the magnitude of axial strain and therefore tension intensity, one radial band was placed midway along the actuators length[35]. By reducing the radial strain at the midpoint of the actuator, this addition meant that higher inflation pressures were realizable. The maximum axial strain achieved experimentally was 9.25% at 71.5kPa. The corresponding numerical axial strain exhibited was 10.77% which shows good agreement.

Radius of curvature was used to characterize the bending actuator. To achieve bending, the actuator's reinforcement layer comprised an inextensible spine (arc length: 14mm) in combination with twenty radial bands spaced along the actuator's length to limit radial expansion on that side of the actuator. The maximum experimentally determined radius of curvature was 42.19mm at 120kPa. This result was closely matched by the FEM model which predicted 42.80mm.

The twisting actuator encompassed twenty helical fibers wound around the circumference of the actuator, each orientated at an angle of 30° to the longitudinal axis. The experimentally determined angle of twist was 102° at 38.26kPa and the corresponding numerical prediction was 130°. This model showed reasonably good correlation between inflation pressure and angle of twist at lower pressures, however convergence issues arose at higher pressures. Physically, this limit may correspond to minimal delamination occurring between the TPE fibers and silicone matrix at increased pressures. Numerically, switching to an explicit solver may be more suitable at higher pressures.

Discrepancies between numerical and experimental results presented are likely due to experimental errors arising from the following sources: the controllable resolution of the analogue pressure regulator; materials testing limited to uniaxial tension (i.e. excluding other deformation modes or viscoelastic properties); and silicone material slippage in the experimental grips. No out of plane

motions were observed in the FE models and all models demonstrated the locations of stress concentration zones which will aid future design optimization.

Conclusions

This article has demonstrated a method of fabricating customizable soft fluidic actuators through additive manufacturing. A composite printing method compatible with thermoset and thermoplastic elastomeric feedstocks including flexible filament and viscous pastes was established by modifying an affordable (€1000) desktop 3D printer; these modifications cost approximately €180. A streamlined algorithm that enables the actuators to be rapidly configured was developed. A demonstration of the speed and flexibility of the system was made by customizing and fabricating contracting, bending, and twisting actuators. Experimental and numerical characterization showed that the proposed manufacturing method can produce actuators with varied motions simply by modifying a small number of actuator parameters.

Future work will aim to further develop this manufacturing method by combining it with results from the literature. For example, Connolly *et al.* presented a kinematic trajectory matching design tool[36] that determines actuator parameters that yield a specific user-defined motion. Combining this design tool with the manufacturing method presented here would automate the end-to-end design and fabrication of mechanically-programmable actuators. The ability to numerically model, digitally configure and directly additively manufacture custom actuators inexpensively could facilitate rapid prototyping of next generation programmable soft robotic devices. In addition, Wyatt *et al.*[37] have demonstrated the potential of "smart braids" for incorporating self-sensing into soft pneumatic actuators; incorporating electrically conductive printing materials into the manufacturing process described here, would allow the direct printing of actuators with embedded sensing.

In a roundtable discussion, Trimmer et al. outlined unmet needs in the soft robotics field, namely; i) having the capability to simulate and design printable actuators, ii) integrating multiple-materials into a single print job, iii) individually addressable multi-nozzle print-heads, iv) fast print-speed, and v)

ways to simulate the interactions of these multi-materials[20]. This work has demonstrated potential ways of achieving such objectives.

Author Disclosure Statement

No competing financial interests exist.

Acknowledgments

This publication has emanated from research supported in part by a research grant from Science Foundation Ireland (SFI) and is co-funded under the European Regional Development Fund under Grant Number 13/RC/2073.

References

1. Galloway KC, Polygerinos P, Walsh CJ, et al. Mechanically Programmable Bend Radius for Fiber-Reinforced Soft Actuators. 2013 16th International Conference on Advanced Robot. (Icar) 2013:6.
2. Polygerinos P, Wang Z, Galloway KC, et al. Soft robotic glove for combined assistance and at-home rehabilitation. Robot. and Autonomous Sys. 2015;73:135-143.
3. Connolly F, Polygerinos P, Walsh CJ, et al. Mechanical Programming of Soft Actuators by Varying Fiber Angle. Soft Robot. 2015;2(1):26-32.
4. Holland DP, Park EJ, Polygerinos P, et al. The Soft Robotics Toolkit: Shared Resources for Research and Design. Soft Robot. 2014;1(3):224-230.
5. Suzumori K, Iikura S, Tanaka H, FLEXIBLE MICROACTUATOR FOR MINIATURE ROBOTS. Ieee Micro Electro Mechanical Systems: an Investigation of Micro Structures, Sensors, Actuators, Machines and Robots 1991:204-209.
6. Panagiotis P, Zheng W, Overvelde JTB, et al. Modeling of Soft Fiber-Reinforced Bending Actuators. IEEE Transactions on Robot. 2015;31(3):778-789.
7. Krishnan G, Bishop-Moser J, Kim C, et al. EVALUATING MOBILITY BEHAVIOR OF FLUID FILLED FIBER-REINFORCED ELASTOMERIC ENCLOSURES. Proceedings of the Asme International Design Engineering Technical Conferences and Computers and Information in Engineering Con. 2012:4, Pts A and B 1089-+.
8. Kim S, Laschi C, Trimmer B. Soft robotics: a bioinspired evolution in robotics. Trends in Biotechnology 2013;31(5):23-30.
9. Martinez RV, Branch JL, Fish CR, et al. Robotic Tentacles with Three-Dimensional Mobility Based on Flexible Elastomers. Advanced Mat. 2013;25(2):205-212.
10. Yi S, Kai YH, Xinquan L, et al. Stiffness Customization and Patterning for Property Modulation of Silicone-Based Soft Pneumatic Actuators. Soft Robot. 2017;4(3):251-260.
11. Roche ET, Horvath MA, Wamala I, et al. Soft robotic sleeve supports heart function. Science Translational Med. 2017;9(373):11.
12. Roche ET, Wohlfarth R, Overvelde JTB, et al. A Bioinspired Soft Actuated Material. Advanced Mat. 2014;26(8):1200-1206.
13. Payne CJ, Wamala I, Abah C, et al. An Implantable Extracardiac Soft Robotic Device for the Failing Heart: Mechanical Coupling and Synchronization. Soft Robot. 2017;4(3):241-250.

14. Gul JZ, Yang YJ, Su KY, et al. Omni Directional Multimaterial Soft Cylindrical Actuator and Its Application as a Steerable Catheter. Soft Robot. 2017;4(3):224-240.
15. X. Liang YS, H. Ren. A Flexible Fabrication Approach Toward the Shape Engineering of Microscale Soft Pneumatic Actuators. IEEE Robotics and Aut. Letters 2017.pp.165-170.
16. Gafford J, Ding Y, Harris A, et al. Shape Deposition Manufacturing of a Soft, Atraumatic, and Deployable Surgical Grasper. Journal of Mechanisms and Robotics-Transactions of the Asme 2015;7 (2):11.
17. Elsayed Y, Vincensi A, Lekakou C, et al. Finite Element Analysis and Design Optimization of a Pneumatically Actuating Silicone Module for Robotic Surgery Applications. Soft Robot. 2014;1 (4):255-262.
18. Sun Y, Song YS, Paik J. Characterization of Silicone Rubber Based Soft Pneumatic Actuators. IEEE/RSJ International Conference on Intelligent Robots and Systems (IROS). 2013.pp.4446-4453.
19. Marchese AD, Katzschmann RK, Rus D. A Recipe for Soft Fluidic Elastomer Robots. Soft Robot. 2015;2(1):7-25.
20. Trimmer B, Lewis JA, Shepherd RF, et al. 3D Printing Soft Materials: What Is Possible? Soft Robot. 2015;2(1):3-6.
21. Truby RL, Lewis JA. Printing soft matter in three dimensions. Nature 2016;540(7633):371-378.
22. Peele BN, Wallin TJ, Zhao H, et al. 3D printing antagonistic systems of artificial muscle using projection stereolithography. Bioinspiration & Biomim. 2015;10(5).
23. Yap HK, Ng HY, Yeow CH. High-Force Soft Printable Pneumatics for Soft Robotic Applications. Soft Robot. 2016;3(3):144-158.
24. MacCurdy R, Katzschmann R, Kim Y, et al. Printable Hydraulics: A Method for Fabricating Robots by 3D Co-Printing Solids and Liquids. IEEE International Conference on Robotics and Auto. (ICRA). 2016.pp.3878-3885.
25. Bartlett NW, Tolley MT, Overvelde JTB, et al. A 3D-printed, functionally graded soft robot powered by combustion. Science 2015;349(6244):161-165.
26. Wehner M, Truby RL, Fitzgerald DJ, et al. An integrated design and fabrication strategy for entirely soft, autonomous robots. Nature 2016;536(7617):451-+.
27. Jahan ZG, Young JY, Kim YS, et al. Omni Directional Multimaterial Soft Cylindrical Actuator and Its Application as a Steerable Catheter. Soft Robot. 2017;4(3):224-240.
28. Coulter FB, Ianakiev A. 4D Printing Inflatable Silicone Structures. 3d Printing and Additive Manufact. 2015;2(3):140-144.
29. Wade G. Direct Drive Extruder. https://www.thingiverse.com/make:33486/. 2013.
30. Ultimaker Original Stock Extruder Parts. https://github.com/Ultimaker/UltimakerOriginal. 2014.
31. Ober TJ, Foresti D, Lewis JA. Active mixing of complex fluids at the microscale. Proceedings of the National Academy of Sciences of the United States of America 2015;112(40):12293-12298.
32. Polygerinos P, Lyne S, Wang Z, et al. Towards a Soft Pneumatic Glove for Hand Rehabilitation. IEEE/RSJ International Conference on Intelligent Robots and Systems (IROS). 2013.pp.1512-1517.
33. Doube M. FitCircle.Java Macro.
https://www.github.com/mdoube/BoneJ/blob/master/src/org/doube/geometry/FitCircle.java. 2016.
34. Dassault Systèmes Simulia Corp. P, RI, USA. 'Abaqus/CAE 6.14 User's Guide/Hyperelastic behavior of rubberlike materials'. Online Documentation. 2014.
35. Park YL, Santos J, Galloway KG, et al. A Soft Wearable Robotic Device for Active Knee Motions using Flat Pneumatic Artificial Muscles. IEEE International Conference on Robotics and Auto. (ICRA). 2014.pp.4805-4810.
36. Connolly F, Walsh CJ, Bertoldi K. Automatic design of fiber-reinforced soft actuators for trajectory matching. Proceedings of the National Academy of Sciences of the United States of America 2017; 114(1):51-56.
37. Wyatt F, Yi Chin K, Remy DC. Smart Braid Feedback for the Closed-Loop Control of Soft Robotic Systems. Soft Robot. 2017;4(3):261-273.

(I) Molding Manufacturing Method

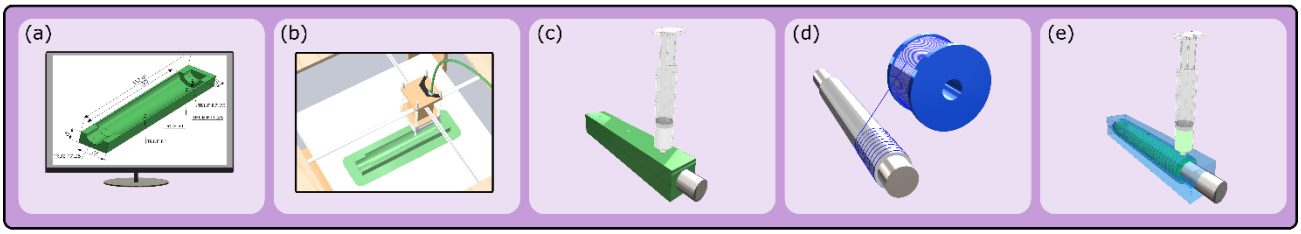

(II) Additive Manufacturing Method

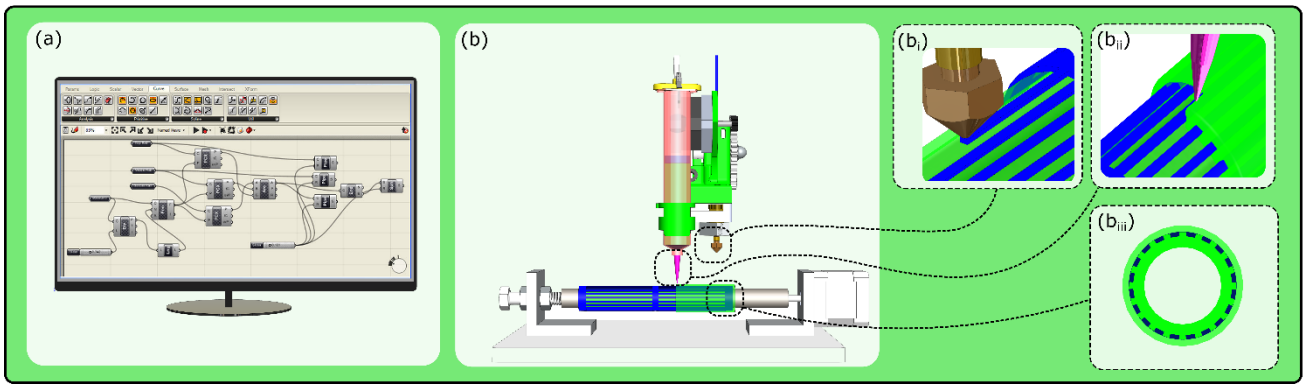

FIG. 1. Schematic of the molding manufacturing method versus additive manufacturing method. **(i.a)** A two-part mold is designed in CAD to accommodate for an axial mandrel core. **(i.b)** The mold parts are 3D printed. **(i.c)** The mold is assembled and silicone is injected into the cavity. **(i.d)** Inextensible fibers are manually wrapped around the cured silicone bladder in predefined grooves. **(i.e)** The actuator's skin layer is formed using a second larger mold (duration [molds already printed]: 5 h). **(ii)** Composite additive manufacture method. **(ii.a)** Design actuator using Grasshopper 3D algorithm. **(ii.b)** The actuator is printed onto a rotating mandrel using a custom-built composite printer (duration: 1 h). **(ii.b_i)** Actuator reinforcement layer deposition. **(ii.b_{ii})** Final silicone skin layer extrusion. **(ii.b_{iii})** Section view of the tubular actuator. TPE reinforcement (blue) is embedded within the silicone matrix (green). 3D, three-dimensional; TPE, thermoplastic elastomer.

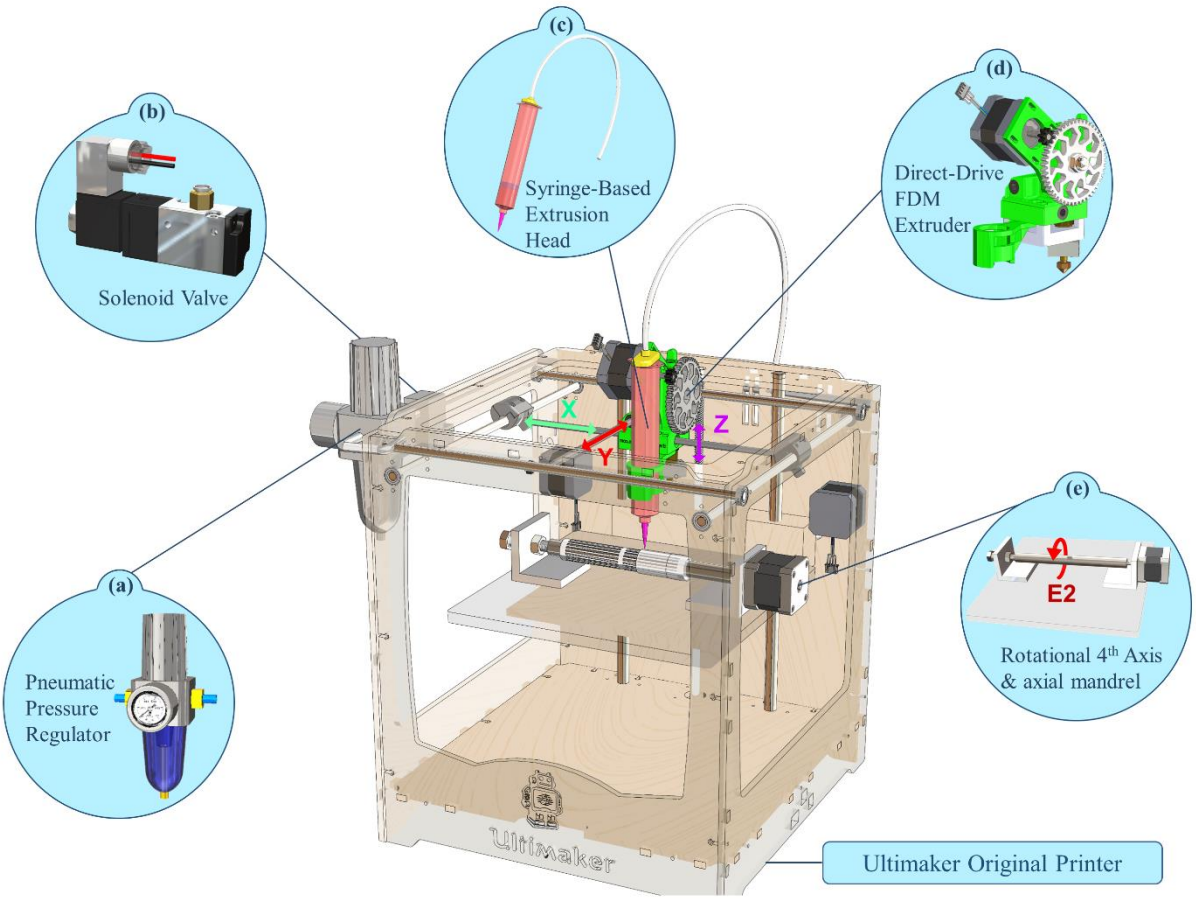

FIG. 2. Perspective view of the Ultimaker Original 3D printer. Hardware modifications highlighted in detail views. **(a)** Pressure regulator to control extrusion pressure. **(b)** Solenoid valve that toggles air ON/OFF. **(c)** Paste extrusion head. Fifty five-cubic centimeter syringe barrel with a 20-gauge luer lock dispensing tip. The syringe barrel is mounted on the printhead using a 3D printed bracket. The on-board syringe removes the need for a material feed line from an off-board syringe, which prevents material wastage. **(d)** Direct-drive FDM printhead with standard 0.4-mm hot end. **(e)** Fourth axis with rotational degree of freedom. Axial 14-mm mandrel coupled to stepper motor. Each axis, namely X, Y, Z, or E2, is individually addressable from the G-code. FDM, fused deposition modeling.

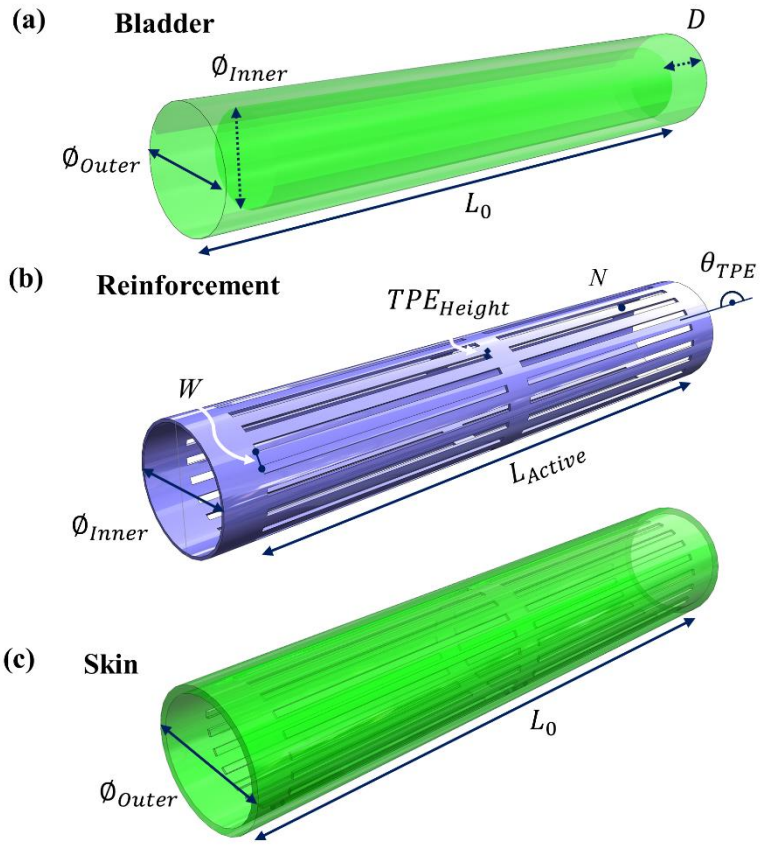

FIG. 3. Exploded view of actuator composition. **(a)** Silicone bladder layer that has been plugged at one end. Concealed 14-mm ϕ cavity. **(b)** Longitudinal TPE reinforcement layer for the contracting actuator. Note: There is one radial band present midway along the actuator's length to increase the actuator's tension intensity. **(c)** Silicone skin layer that serves to encapsulate the fibers and increase the actuator's structural integrity.

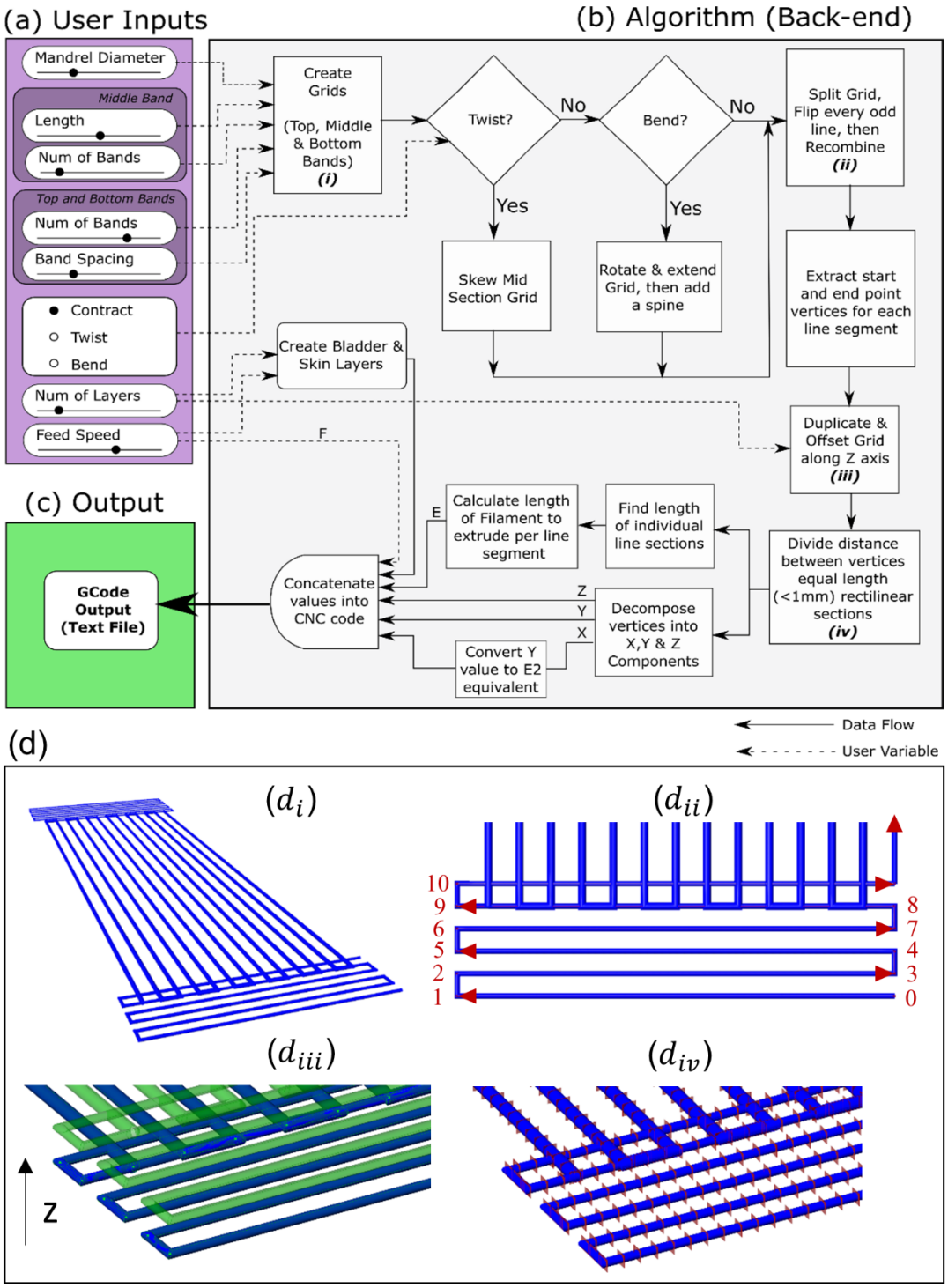

FIG. 4. Schematic of actuator design algorithm. **(a)** Front-end partition of algorithm comprising user inputs that control the parametric properties of the actuator. These inputs are easily adjusted using number sliders. **(b)** Back-end partition of algorithm. This portion of the algorithm comprises predefined functions that utilize input parameters to create a toolpath for each actuator layer, which will be 3D printed later **(c).** Algorithm output. The algorithm automatically streams an output Gcode text file. **(d)** Visualization of output in RhinoCAD workspace. **(d_i)** The reinforcement layer is created by combining rectangular grids for each actuator section. **(d_{ii})** A continuous toolpath that connects all the vertices of grids is generated. **(d_{iii})** A multilayered toolpath is generated. **(d_{iv})** Toolpath subdivision is executed to automate extrusion quantity calculation.

Table 1. Actuator Parameters (Contraction Design)

(a) Bladder Layer	Dimension
$\emptyset_{Inner}$ (Cavity)	14mm
$\emptyset_{Outer}$	18mm
L_0	115mm
D (End Plug Depth)	6mm
(b) Reinforcement Layer	
$\emptyset_{Inner}$	18mm
Layer Height	0.5mm
Number of Layers	2
TPE_{Height}	1mm
W (Fibre Width)	1.85mm
θ_{TPE}	0^0
N (Number of Fibres)	20
Middle Band Width	4mm
End Band Width	7.5mm
L_{Active} (Active Length)	100mm
(c) Skin Layer	
$\emptyset_{Outer}$	22mm
L_0	115mm

Table 2. Material Parameters

Dragon Skin 10 Silicone (Thermoset)	
Shore Hardness	10A
Mixed Viscosity	23Pas
Plat-Cat Cure Accelerator Added by Weight to Part 'A'	4%
Pot Life (Including Plat-Cat)	10min
Cure Time (heat accelerated)	4min
Elongation at break	1000%
Density	1170.18kg/m^3
TPE (Thermoplastic elastomer)	
Shore Hardness	93A
Filament Diameter Accuracy	2.9-3mm
Density	900kg/m^3
Melt Flow Index, 200°C/5kg	11g/10min
Heat Distortion Temp	70°C
Tensile Strength	11.8MPa
Tensile Elongation	500%
Nozzle Temp	190-240°C

Table 3. Printing Parameters

Bladder Layer	
Weight	30g
Extrusion Pressure	500kPa
Mandrel Rotational Speed	20rpm
Print Time & Curing	6min
Reinforcement Layer	
Hot-End Temperature	235℃
Nozzle Size	0.4mm
Layer Height	0.5mm
Extrude Rate E1 (Length of Filament Drawn in)	0.098mm/mm
Print Speed	100mm/min
Print Duration	45min
Skin Layer	
Weight	18g
Extrusion Pressure	500kPa
Print Time & Curing	6min
Total Print Time	1hour

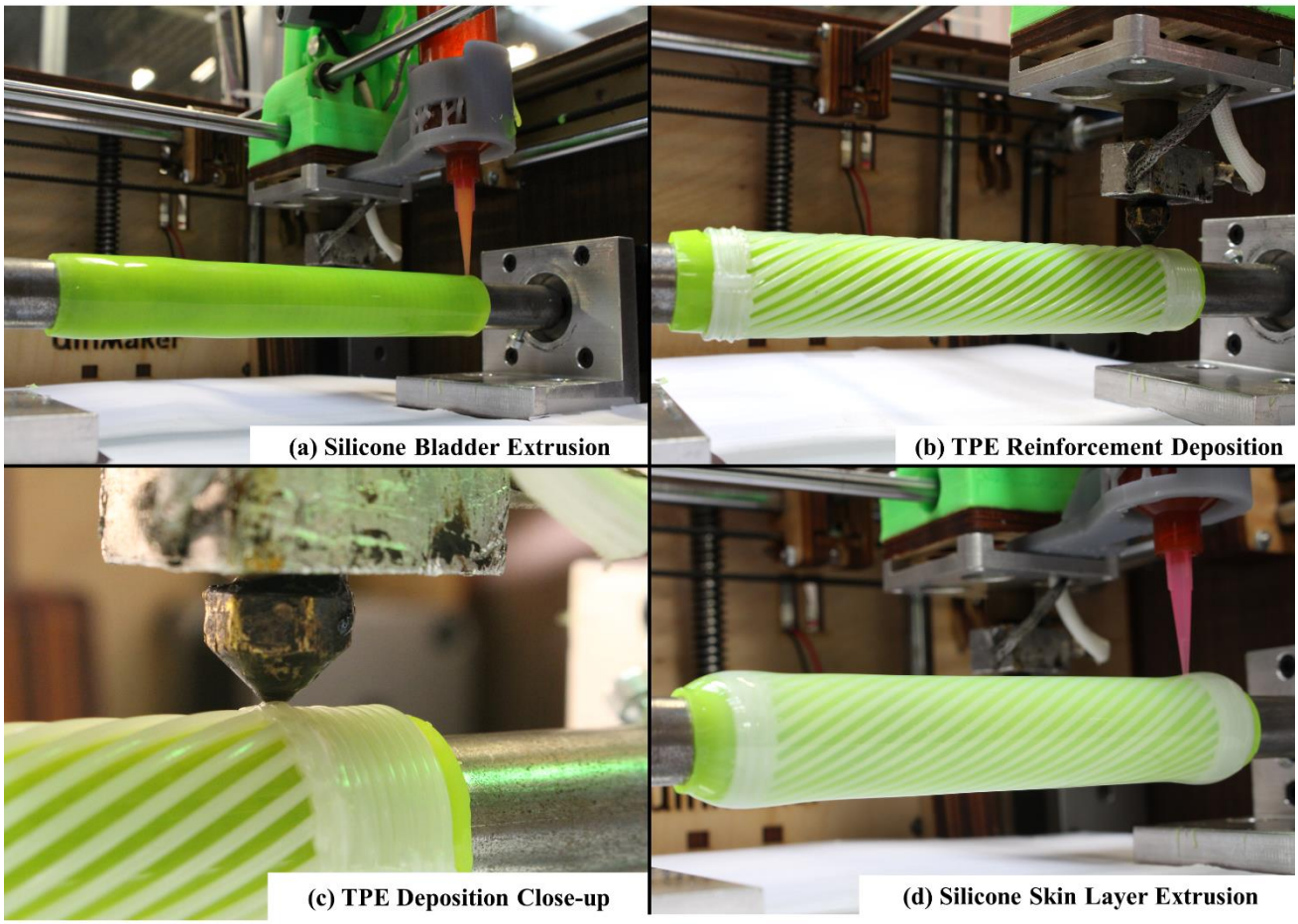

FIG. 5. Additive manufacture of twisting actuator. **(a)** Silicone bladder extrusion onto rotating mandrel. **(b)** TPE deposition onto silicone bladder with end-bands laterally. **(c)** Close-up of TPE deposition. The FDM printhead is completing the second layer of TPE deposition. **(d)** Transparent silicone skin layer extrusion over previous two layers.

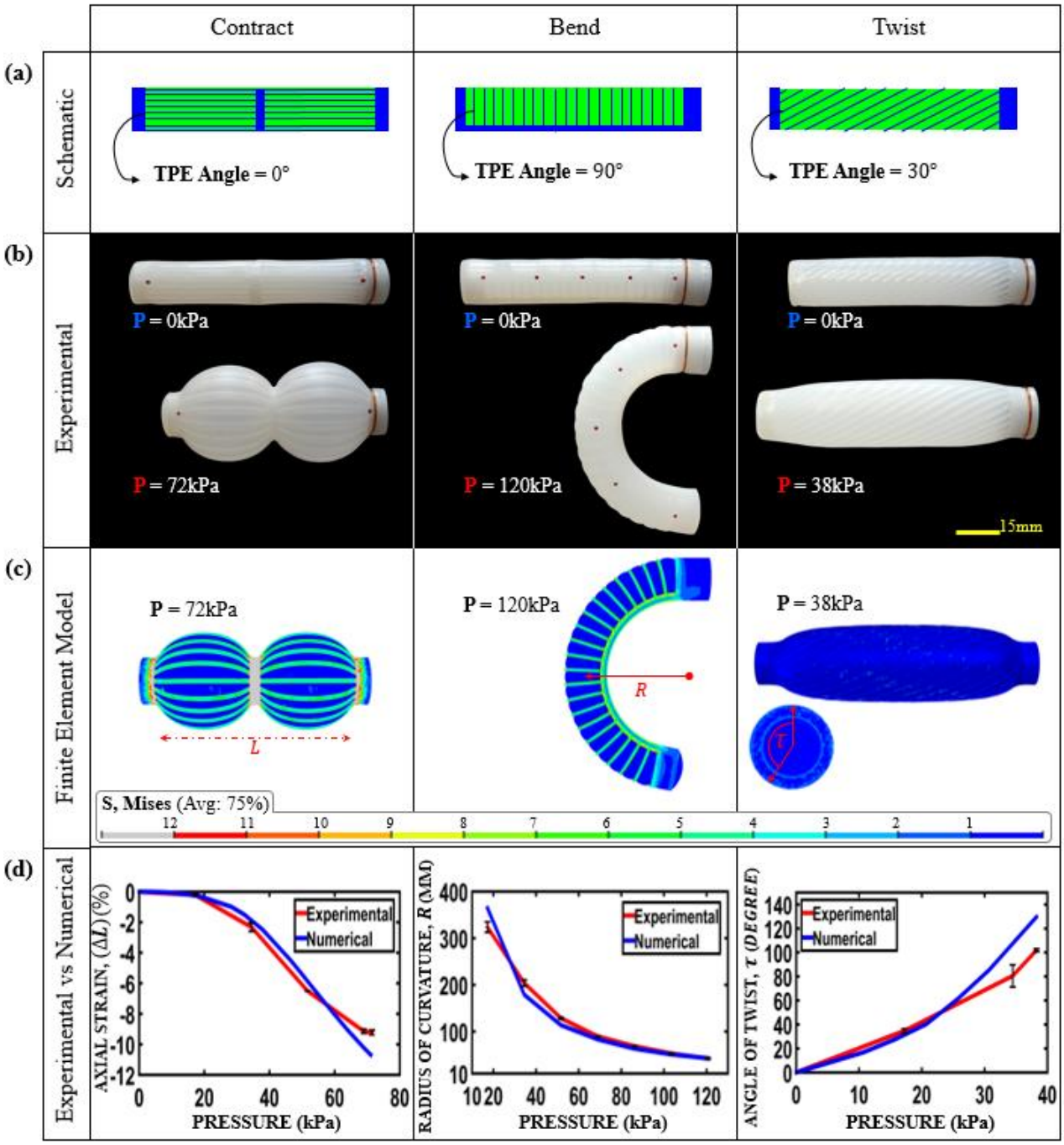

FIG. 6. Experimental and numerical results. **(a)** *Row* 1: TPE reinforcement layer arrangement for contracting, bending, and twisting actuator designs. **(b)** *Row* 2: Physical models of the same actuators in their deflated (upper image) and inflated states (lower) at maximum pressure. Fiducial markers are glued to the actuators' surfaces in strategic locations for displacement tracking. **(c)** *Row* 3: Finite element models of actuators highlighting the stress concentration zones (Note: the skin layer is removed from each model image for the purpose of visualizing Von Mises stress distribution in the fibers). **(d)** *Row* 4: Experimental and numerical result comparison as a function of pressure (kPa). Axial strain ε (%) is plotted for the contraction actuator. Radius of curvature R (mm) is plotted for the bending actuator. Angle of twist τ (°) is plotted for the twisting actuator. Error bars on the experimental results illustrate the standard deviation from the mean result obtained after three consecutive tests on each actuator type.

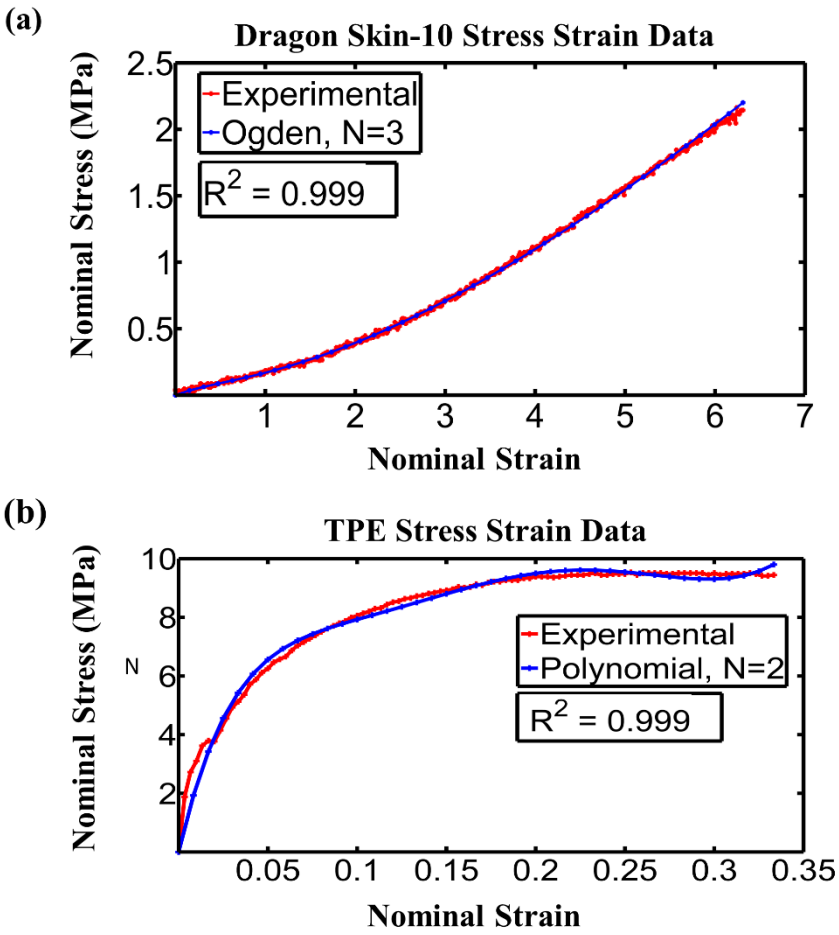

FIG. 7. Experimental vs. numerical stress–strain relationships. **(a)** Average nominal stress–strain experimental relationship for Dragon Skin 10 (*red*). Ogden, $N = 3$ strain energy function fit (*blue*). **(b)** Average nominal stress–strain experimental relationship for TPE (*red*). Polynomial, $N= 2$ strain energy function fit (*blue*).

Table 4. Hyperelastic Model Parameters for Dragon Skin 10 and Thermoplastic Elastomer Materials

Dragon Skin 10 Strain Energy Function Coefficient	**Ogden, N=3 Model Parameter Values**
I_1: μ_1	-1.82613311 (MPa)
I_1: α_1	1.61311930
I_2: μ_2	1.12017964 (MPa)
I_2: α_2	2.01841646
I_3: μ_3	0.795105621 (MPa)
I_3: α_3	0.938645449
TPE Strain Energy Function Coefficient	**Polynomial, N = 2 Model Parameter Values (MPa)**
C_{10}	-571.204963
C_{01}	614.992755
C_{20}	3355.09691
C_{11}	-8975.24336
C_{02}	6339.02858

Table 5. Actuator Geometric Parameters and Interlayer Constraints for Bending, Twisting, and Contracting Actuator Designs.

Actuator Type and Constituent Part	**Number of Nodes**	**Number of Elements (C3D10H)**	**Surface Pairs**	**Constraint Type**
Bend				
• Bladder	60171	36908	Bladder – TPE	Tie Constraint
• TPE Fibres	51017	24240	TPE - Skin	Contact Interaction
• Skin Layer	85153	50409	Bladder – Skin	Tie Constraint
Twist				
• Bladder	57196	34875	Bladder – TPE	Contact Interaction
• TPE Fibres	88947	42517	TPE - Skin	Contact Interaction
• Skin Layer	67381	33753	Bladder – Skin	Contact Interaction
Contract				
• Bladder	14178	7781	Bladder – TPE	Tie Constraint
• TPE Fibres	29043	13254	TPE - Skin	Contact Interaction
• Skin Layer	37187	18551	Bladder – Skin	Tie Constraint